

## PHOTOEVAPORATION OF CIRCUMSTELLAR DISKS AROUND YOUNG STARS

ANDREEA S. FONT,<sup>1</sup> IAN G. MCCARTHY,<sup>1</sup> DOUG JOHNSTONE,<sup>1,2</sup> AND DAVID R. BALLANTYNE<sup>3</sup>

*Received 2003 October 6; accepted 2004 February 10*

### ABSTRACT

We examine the ability of photoevaporative disk winds to explain the low-velocity components observed in the forbidden line spectra of low-mass T Tauri stars. Using the analytic model of Shu and coworkers and Hollenbach and coworkers as a basis, we examine the characteristics of photoevaporative outflows with hydrodynamic simulations. General results from the simulations agree well with the analytic predictions, although some small differences are present. Most importantly, the flow of material from the disk surface develops at smaller radii than in the analytic approximations, and the flow velocity from the disk surface is only one-third the sound speed. A detailed presentation of observational consequences of the model is given, including predicted line widths, blueshifts, and integrated luminosities of observable sulfur and nitrogen emission lines. We demonstrate that these predictions are in agreement with current observational data on the low-velocity forbidden line emission of ionized species from T Tauri stars. This is in contrast to magnetic wind models, which systematically underpredict these forbidden line luminosities. However, the present model cannot easily account for the luminosities of neutral oxygen lines in T Tauri stars.

*Subject headings:* accretion, accretion disks — hydrodynamics — stars: formation

### 1. INTRODUCTION

It is now generally accepted that most young, low-mass stars are born with circumstellar disks and that the evolution of these disks holds a key to planet formation. Observational evidence for circumstellar disks takes many forms, from direct imaging (e.g., Jayawardhana et al. 2002) and imaging of disk silhouettes (e.g., Bally et al. 2000) to indirect measurements such as infrared excess (e.g., Lada et al. 2000). These data provide an estimate for the lifetime of disks around low-mass stars,  $\tau_{\text{disk}} \sim 6 \times 10^6$  yr (Haisch et al. 2001), requiring the presence of an efficient disk dispersal mechanism.

Hollenbach et al. (2000) considered a variety of disk dispersal mechanisms and concluded that viscous accretion of the disk onto the central star (e.g., Hartmann et al. 1998), although it dominates erosion of the inner disk, is incapable of removing the entire disk mass in the required time. Alternatively, photoevaporation of the disk, while providing an effective mechanism for disk removal at large radii  $\gtrsim 10$  AU, cannot remove the inner material (Shu et al. 1993, hereafter SJH93; Hollenbach et al. 1994, hereafter HJLS94; Johnstone et al. 1998). Acting together, viscous accretion and photoevaporation were predicted to efficiently remove the entire disk. Numerical calculations by Clarke et al. (2001) and Matsuyama et al. (2003a) have shown that the combined effects of photoevaporation and viscous accretion are capable of dispersing disks on  $10^5$ – $10^7$  yr timescales. In addition, the formation of gaps within the gaseous disk during the dispersal era may place constraints on the evolution of planetary orbits (Matsuyama et al. 2003b).

The photoevaporation model for disk dispersal has been shown to fit the observational data well in the case of external

heating via nearby massive stars (Bally et al. 1998; Johnstone et al. 1998; Störzer & Hollenbach 1998). However, with the exception of a few cases (e.g., MWC 349A), evidence for disk photoevaporation due to heating from the central star (SJH93; HJLS94) is largely circumstantial. Low-velocity ( $\sim 10$  km s<sup>-1</sup>), blueshifted forbidden lines observed in the spectra of T Tauri stars (Hartigan et al. 1995, hereafter HEG95) may provide evidence for the  $10^4$  K thermal disk winds expected in the photoevaporation model. The theoretical models of SJH93 and HJLS94 do not, however, include detailed hydrodynamic calculations, and thus it has not been possible to test the model directly against these observations.

In this paper we take a first look at the hydrodynamic flow of thermally driven disk winds powered by photoevaporative heating in order to determine the observational consequences of the photoevaporation model. We begin in § 2 with a brief description of how photoevaporation works, concentrating on photoevaporation due to heating from a star at the center of the disk. In § 3 we describe how the hydrodynamic simulations are performed and their results. The predicted observable properties of the simulations are presented in § 4 and are compared with existing data. Further discussion and conclusions are presented in § 5.

### 2. PHOTOEVAPORATION OF CIRCUMSTELLAR DISKS

Photoevaporation of disks by ionizing photons is a conceptually simple process to understand: high-energy radiation (e.g., EUV, X-rays) from the central star ionizes hydrogen at the disk surface, producing a hot  $10^4$  K ionized layer, similar to H II region conditions. Near the star this coronal zone above the disk is expected to be almost static and bound to the disk because of its location deep in the potential well of the star; however, at large radii from the star the thermal layer should be unbound, powering a thermally driven disk wind. The critical length scale for the model is given in SJH93 and HJLS94 by

$$r_g = \frac{GM_*}{c_s^2}, \quad (1)$$

<sup>1</sup> Department of Physics and Astronomy, University of Victoria, Victoria, BC V8P 1A1, Canada; afont@uvastro.phys.uvic.ca, mccarthy@uvastro.phys.uvic.ca.

<sup>2</sup> National Research Council of Canada, Herzberg Institute of Astrophysics, 5071 West Saanich Road, Victoria, BC V9E 2E7, Canada; doug.johnstone@nrc-cnrc.gc.ca.

<sup>3</sup> Canadian Institute for Theoretical Astrophysics, 60 St. George Street, Toronto, ON M5S 3H8, Canada; ballantyne@cita.utoronto.ca.

where  $M_*$  is the mass of the star and  $c_s \sim 10 \text{ km s}^{-1}$  is the sound speed of the ionized gas.

In order to determine the number density of hydrogen atoms at the base of the ionized layer, SJH93 and HJLS94 assume that for  $r < r_g$  the atmosphere is in hydrostatic equilibrium such that

$$n(r, z) = n_0(r) \exp\left[-\frac{z^2}{2H(r)^2}\right], \quad r < r_g, \quad (2)$$

where  $z$  is the height above the disk and  $H(r)$  is the scale height:

$$H(r) = r_g \left(\frac{r}{r_g}\right)^{3/2}, \quad r < r_g. \quad (3)$$

The ionization of the material above the disk is not dominated by the direct passage of EUV photons from the central star but rather through the indirect EUV photons produced by recombination within the ionized layer. This effective scattering is strong because one in three recombinations goes directly to the ground state, producing a new Lyman continuum photon. The angular scale height, as seen from the central star, grows with distance from the disk center, enabling the top of the ionized atmosphere to intercept direct EUV photons and redirect these photons through recombinations downward (and upward). Analytic analysis and numerical computation (HJLS94) allow for a determination of the base density power-law profile:

$$n_0(r) = n_g \left(\frac{r}{r_g}\right)^{-3/2}, \quad r < r_g, \quad (4)$$

where

$$n_g = C \left(\frac{3\Phi_*}{4\pi\alpha_2 r_g^3}\right)^{1/2}. \quad (5)$$

In the above,  $\alpha_2$  is the recombination coefficient for all states except the ground state, and  $\Phi_*$  is the ionizing (EUV) photon flux from the central star. Numerical analysis fixes the order of unity constant to be  $C = 0.1$ .

At radii larger than  $r_g$ , the ionized layer is assumed to flow at approximately the sound speed, and thus the scale height takes the form

$$H(r) = r, \quad r > r_g. \quad (6)$$

In this case the angular scale height is constant, and the atmosphere directly above the disk no longer has a clear line of sight to the central star; therefore, the density at the base of the atmosphere decreases much more quickly than within  $r_g$ :

$$n_0(r) = n_g \left(\frac{r}{r_g}\right)^{-5/2}, \quad r > r_g. \quad (7)$$

The mass-loss rate due to the flow from both sides of the disk, as a function of disk radius, can then be computed directly:

$$\frac{d\dot{M}_{\text{dw}}}{dr} = 4\pi r n_0(r) c_s m_{\text{H}}, \quad r > r_g, \quad (8)$$

where  $m_{\text{H}} = 1.35m_{\text{H}}$  is the mean mass per hydrogen atom.

Only two parameters are required to fully specify the photoevaporation model:  $M_*$  and  $\Phi_*$ . HJLS94 examined the effects of photoevaporation of the circumstellar disk around massive stars where the ionizing flux  $\Phi_*(M_*)$  is set by the mass of the star. SJH93, however, considered the effects of photoevaporation of the circumstellar disk around low-mass stars and concluded that only during the early T Tauri stage, when the star disk accretion shock produces enhanced EUV radiation, would photoevaporation be important. Matsuyama et al. (2003a) self-consistently computed the strength of the star disk accretion shock during the dispersal of the disk and concluded that high ionization rates,  $\Phi_* > 10^{40} \text{ s}^{-1}$ , are expected for the initial  $\sim 10^6$  yr. Recently, doubts have been raised about the possibility of ionizing radiation penetrating the thick protostellar jet, which lies between the star and the disk (Shang et al. 2002). In addition, the accretion shock itself may be thick to ionizing radiation (Alexander et al. 2004). In this paper we assume that a strong ionizing radiation field is present, from either the accretion shock, the chromospherically active star, or some other radiation-generating process associated with accretion and the release of potential energy.

A modified photoevaporation model for disk dispersal is applicable to situations in which the low-mass stars with disks are located near massive stars, such as in the Orion Trapezium. Johnstone et al. (1998) showed that in such cases the geometry for both the radiative transfer of the ionizing radiation and the hydrodynamic flow is much simpler, and the model results provide a good match to the observations. However, it is clear that such external evaporation is not applicable to every low-mass star. In the case of photoevaporation due to an isolated central star, detailed fits to the observational data have not been possible because of the poor understanding of the flow characteristics. However, there are clear strengths to such a model, including the ability to disperse the disk on the observationally determined timescale (SJH93; Hollenbach et al. 2000; Matsuyama et al. 2003a) and the ability to produce a thermally driven wind with characteristic speed  $c_s$  similar to the low-velocity, blueshifted forbidden line value observed in T Tauri star spectra (HEG95). The photoevaporation model also requires only a few free parameters, and thus the observational characteristics should be well determined. This aspect of the model is in direct contrast to the magnetic wind calculations often used to explain the low-velocity, blueshifted forbidden line radiation (Cabrit et al. 1999; Garcia et al. 2001a, 2001b).

### 3. HYDRODYNAMIC DISK WIND MODELS

As discussed in § 2, a detailed and complete picture of the thermal disk wind can only be attained by explicitly solving for the hydrodynamic flow characteristics. For this purpose, we make use of the publicly available ZEUS-2D hydrodynamic code (Stone & Norman 1992a, 1992b; Stone et al. 1992). This code has been used in previous studies of disk outflows (e.g., Lee et al. 2001) and is a good choice because of its great flexibility in terms of geometry and grid spacing.

The effects of magnetic fields, radiation, radiative transfer, dust, and self-gravity of the gas are neglected in these models. We also neglect the effects of a stellar wind or an inner jet on the dynamics of the flow. A discussion of how this omission could potentially influence our results and conclusions is provided in § 5.

#### 3.1. A Spherical Test: The Parker Wind Problem

Before moving on to the problem of winds from photoevaporating circumstellar disks, it is instructive to consider a

simpler problem to test the method. The Parker solar wind problem (Parker 1963) is ideal for this purpose because it is a transonic outflow problem with a known solution. The Parker wind problem considers the outflow properties of a thermally driven spherically symmetric wind from a gravitating point mass (such as the Sun). Assuming the wind is isothermal and barotropic (i.e., the pressure exerted on the gas is a function of density only), then there is a well-defined analytic solution with the wind passing through a sonic point ( $|v|/c_s = 1$ ) at the radius  $r/r_g = 1/2$ .

To set up the problem in ZEUS-2D, a simple spherical coordinate grid is utilized. The radial coordinate, which is chosen to span  $r/r_g = 0.1-1.0$ , is divided linearly into 100 cells, while the polar coordinate, for which the range  $\theta = 0^\circ-90^\circ$  is used, is divided linearly into 60 cells. The flow is assumed to be azimuthally symmetric in ZEUS-2D. The boundary conditions of the simulation are all made to be reflecting except for the outer radial boundary, which is set as an outflow boundary, and the inner boundary, which is continually updated such that the density remains constant along the inner edge (representing the source of the wind, i.e., near the surface of the star). The density at this inner edge is normalized to 1, while the remainder of the cells in the grid are set to an initial density of  $10^{-4}$ . The initial velocity within each cell is set to zero and the simulation is allowed to run until it reaches steady state. In practice, the velocity of the gas as a function of radius and time is tracked, and we verify that the simulation converges rapidly to a steady state solution identical (to within a few percent accuracy) to the analytic solution, with the sonic point occurring at  $r/r_g = 1/2$ . Since the simulation setup just presented is very similar to the required setup for the disk wind models discussed below, the Parker wind analysis provides a good test of their reliability.

### 3.2. A Disk Wind Test: Power-Law Models

Below we explore winds originating from simple power-law disk models. Before proceeding, we emphasize here that these models are of academic interest only. Our purpose is to examine and understand the character of their solutions. This, in turn, provides a further test of our methods and also gives a basis for understanding the more realistic hybrid case considered below.

#### 3.2.1. Setup

We now consider winds from photoevaporating disks. First, a description is given of the simulation setup in ZEUS-2D and how the models are initialized.

At large radii the flow is expected to be dominated by pressure gradients in the diverging flow and should asymptotically become radial. Therefore, a spherical polar coordinate system is selected for these simulations. Since it is not known a priori where the flow will become sonic, the radial coordinate spans a large range,  $r/r_g = 0.1-20$ , and is divided logarithmically into 200 cells. The polar coordinate is chosen to span the range  $\theta = 0^\circ-90^\circ$  (thus, we are simulating just one quadrant of the atmosphere) and is divided linearly into 100 cells. By using this setup, we avoid excessive computation times but still have high enough resolution near the base, where the pressure gradients are largest, to accurately capture the dynamics of the flow.

Similarly to the Parker wind model described above, all the boundaries are made to be reflecting except for the outer radial boundary, which is an outflow boundary, and the disk base,

which is updated after each time step to the original density distribution (representing replenishment from the photoevaporation of the neutral disk). The disk directly below the ionized atmosphere is assumed to be an infinitely flat, large (i.e., occupying the entire base of the grid) reservoir of neutral material. The base density in the ionized atmosphere is initially set up as a simple power-law distribution with

$$n_0(r) = n_g \left( \frac{r}{r_g} \right)^{-\alpha}, \quad (9)$$

where  $\alpha = 3/2$  or  $5/2$  is the power-law index, spanning the range of model conditions (i.e., eqs. [4] and [7]).

The ionized disk surface is laid down on the equatorial axis ( $\theta = 90^\circ$ ), and the density of the disk (and the above atmosphere) is normalized such that  $n_g = 1$ . The disk is assigned no velocity except for a Keplerian angular velocity. As done for the Parker wind problem, the remaining cells, which comprise the “atmosphere,” are initially filled with a low-density ( $10^{-4}n_g$ ) gas and are assigned no velocity. The results of the simulation are not at all sensitive to the exact value of this density. The simulations are allowed to run until they reach steady state solutions.

#### 3.2.2. Disk Wind Test Results

Plotted in Figures 1 (*left*) and 2 (*left*) are steady state streamlines and velocity contours for the two test cases  $\alpha = 3/2$  and  $5/2$ . The streamlines (*solid lines*) are lines of constant angular momentum  $j_\phi$  (which is a conserved quantity) and demonstrate how the ionized gas flows from the disk. They are spaced in Figures 1 and 2 according to the total disk wind mass-loss rate,  $\dot{M}_{\text{dw,tot}}$  (see the legend of Fig. 1). A comparison of the two figures clearly shows that a much larger fraction of the total mass loss comes from the central regions of the  $\alpha = 5/2$  case than of the  $\alpha = 3/2$  case. Furthermore, the streamlines in the  $\alpha = 5/2$  case are approximately radial, whereas the streamlines in the  $\alpha = 3/2$  case contain a more significant vertical component.

The differences in the spacings and directions of the streamlines of the two cases can be understood physically. Since the  $\alpha = 5/2$  case has a steeper base density profile than the  $\alpha = 3/2$  case, a larger fraction of the ionized gas mass is located within the central region of that model. Indeed,  $\sim 90\%$  of the total mass loss comes from inside  $r_g$  for the  $\alpha = 5/2$  case. In addition, because the  $\alpha = 5/2$  case has a steeper density profile, this necessarily implies that it has a steeper pressure gradient as well. The steeper pressure gradient forces the streamlines to bend more quickly with respect to the vertical direction, producing a more spherical outflow.

The dashed lines in Figures 1 (*left*) and 2 (*left*) represent total velocity  $[v_{\text{tot}} = (v_\theta^2 + v_r^2)^{1/2}]$  contours. The lines demonstrate where  $v_{\text{tot}}$  is equal to  $c_s$ ,  $2c_s$ , and  $3c_s$ . It is clear that the gas flows off the disk in the  $\alpha = 5/2$  case much faster than in the  $\alpha = 3/2$  case, which is directly related to the pressure gradients acting on the system.

Intimately linked with the velocity and streamline properties is the atmosphere density distribution. Plotted in Figures 1 (*right*) and 2 (*right*) are density contours for the two cases. The contours are evenly spaced in log-space and range from  $\log n/n_g = -2.5$  to 0. The  $\alpha = 3/2$  case shows horizontally elongated contours, while the  $\alpha = 5/2$  case shows nearly spherical contours. Again, the difference arises because the  $\alpha = 3/2$  case has an appreciable mass-loss rate even at large

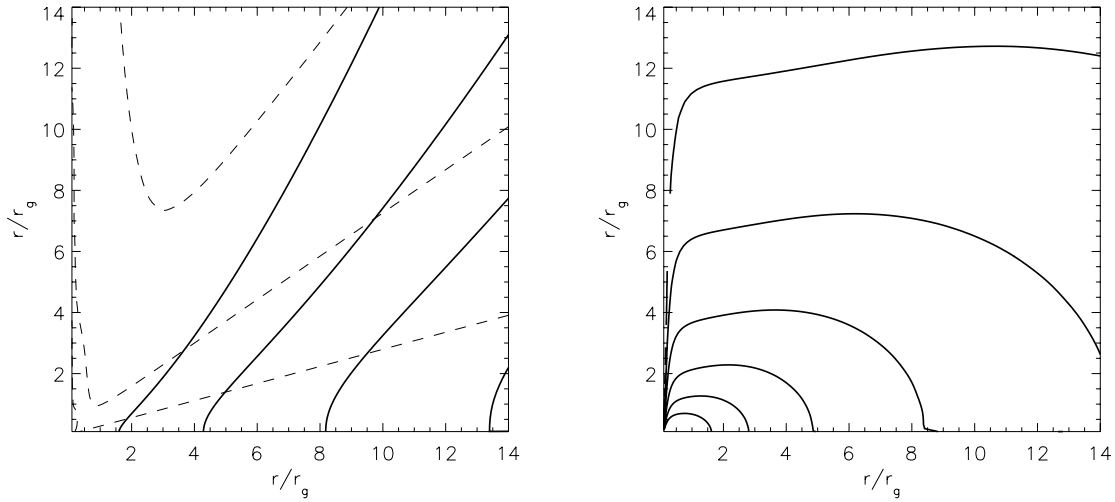


FIG. 1.—Steady state results for the  $\alpha = 3/2$  case. *Left*: Streamline and velocity contours. The solid lines show streamlines and indicate how the ionized gas flows off the disk. They are spaced evenly according to the total mass-loss rate. Namely, the streamlines enclose 20%, 40%, 60%, 80%, and 95% (not shown) of  $\dot{M}_{\text{dw,tot}}$ . The dashed lines indicate where  $v_{\text{tot}}$  equals 1, 2, and 3 times the sound speed (with the velocity of the flow increasing with distance from the disk). *Right*: Density contours. Contours are evenly separated in log-space and range from  $\log n/n_g = -2.5$  to 0.

radii, while the  $\alpha = 5/2$  case has almost no mass loss at large radii.

The small irregularities visible at large radii (near the base) in the  $\alpha = 5/2$  case are transient phenomena (not steady state) and are due to the fact that the density of the base at these radii is comparable to that of the outflowing atmosphere and, therefore, that the flow is easily disrupted. The low densities and mass-loss rates at these radii, however, ensure that these irregularities have little or no effect on the rest of the (steady state) atmosphere or on the predicted observable properties of these models.

### 3.2.3. A Truncated Disk

Figure 1 illustrates that a significant fraction of the total mass-loss rate for the  $\alpha = 3/2$  case originates at large radii. This gives rise to the elongated density contours shown in Figure 1 (*right*). Furthermore, because of the shallow pressure profile of the ionized disk wind, the streamlines show large vertical components (i.e., perpendicular to the disk). We test these ideas quantitatively by running another  $\alpha = 3/2$  simulation, but this time with the disk truncated at  $r/r_g = 5$ . If the

reasoning above is correct, we should expect the density contours for the truncated case to be more spherically symmetric, while streamlines originating near the truncation radius should show greatly reduced vertical components (as there is no force at large radii pushing the gas vertically).

Plotted in Figure 3 are the streamlines and velocity and density contours for the truncated  $\alpha = 3/2$  case. As expected, the streamlines (Fig. 3, *left*) illustrate that the flow becomes approximately radial at large radii. Of note is the streamline that encloses 95% of the total mass-loss rate (and originates quite close to the truncation radius), which is essentially parallel to the ionized disk. Moreover, the density contours (Fig. 3, *right*) also show a more spherical outflow than for the original  $\alpha = 3/2$  case plotted in Figure 1 (*right*). At large radii, the flow tends to spherical symmetry.

### 3.2.4. Comparison with the Parker Wind

In the  $\alpha = 3/2$  case the disk mass loss is dominated by loss from the disk at large distances from the central star, producing a non-spherically symmetric outflow even at large radii. Alternatively, in the  $\alpha = 5/2$  case the disk mass loss is

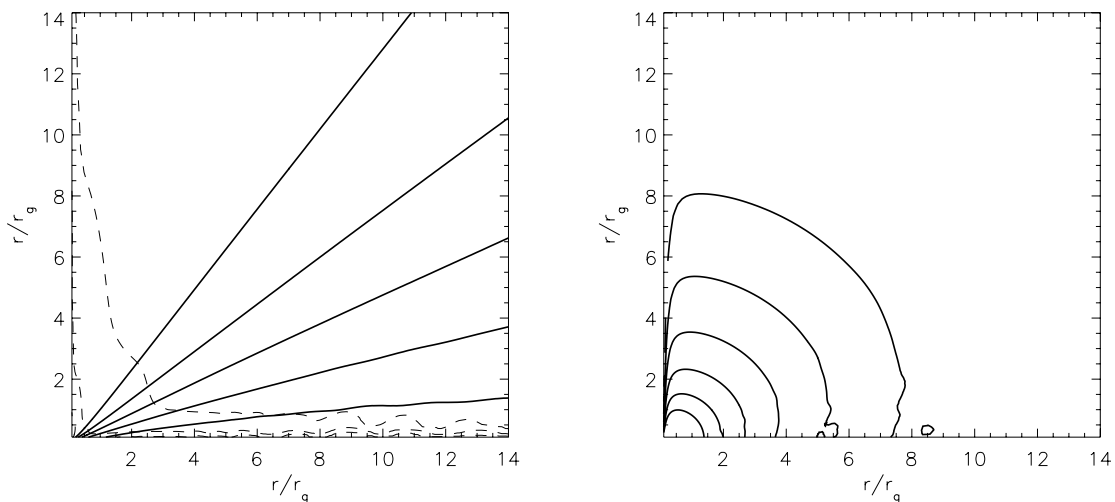


FIG. 2.—Steady state results for the  $\alpha = 5/2$  case. The panels and lines have the same meaning as in Fig. 1.

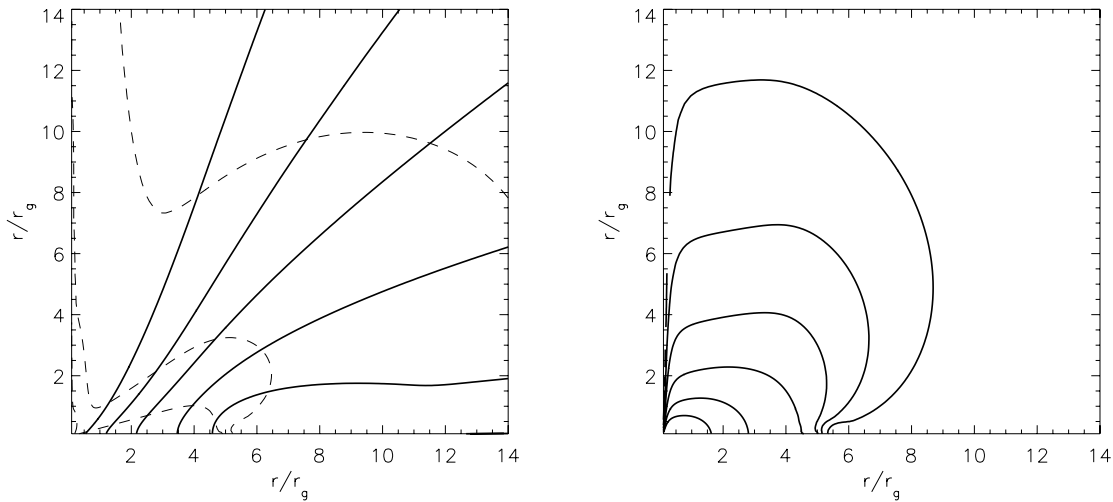


FIG. 3.—Steady state results for the truncated  $\alpha = 3/2$  case. The ionized disk has been truncated at  $r/r_g = 5$ . The panels and lines have the same meaning as in Fig. 1.

dominated by the central region, and the far-field limit tends to spherical symmetry. Comparison of the evaporating disk results with the analytic Parker wind solution provides an ideal framework for understanding the hydrodynamic flow.

In Figure 4 the velocity and density profiles of the two cases are compared with the analytic solution to the Parker wind problem (assuming isothermal, barotropic gas). The simulation profiles are derived at a fixed polar coordinate  $\theta = 45^\circ$  but could just as easily have been chosen from any other slice through the atmosphere (except near the extremes,  $\theta \approx 0^\circ$  or  $90^\circ$ ).

The results plotted in Figure 4 (*left*) clearly indicate that the shape of the velocity profile for the  $\alpha = 5/2$  case closely matches that of the Parker wind solution, including the normalization. The  $\alpha = 3/2$  case, however, has a much different shape and normalization from the Parker wind profile. This simply reflects the fact the  $\alpha = 3/2$  case has a significant mass-loss rate even at large radii, and the pressure forces from

this gas are still modifying the dynamics of the flow (i.e., it is not yet dominated by spherical divergence).

Figure 4 (*right*) illustrates that the flow from the  $\alpha = 5/2$  case is thermally driven at large radii. For  $r \gtrsim r_g$ , the density scales almost exactly as  $r^{-2}$ , as expected for a thermally driven flow (see the Parker wind line, for example). The  $\alpha = 3/2$  case, however, shows an overdense flow at large radii with respect to the other cases. Again, this may be attributed to the non-negligible mass-loss rate at large radii in this case.

### 3.2.5. Comparison with the Analytic Model

The simulations behave as expected, at least at large radii, and we are now in a position to compare the steady state properties with the model of SJH93 and HJLS94 (from which we derive our physically motivated initial conditions). As discussed in § 2, hydrodynamic simulations, such as those performed here, are required for a proper treatment of the flow dynamics. Thus, the model of SJH93 and HJLS94 incorporated

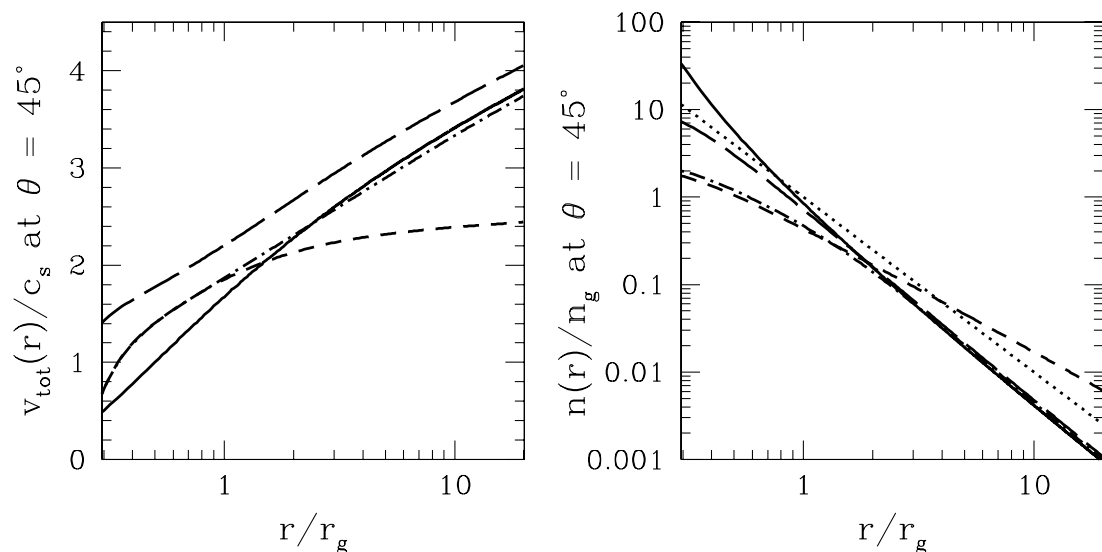


FIG. 4.—Velocity and density profiles at  $\theta = 45^\circ$ . *Left*: Velocity profiles. *Right*: Density profiles. The short-dashed line represents the  $\alpha = 3/2$  case, the long-dashed line represents the  $\alpha = 5/2$  case, and the dot-dashed line represents the PDW model (see § 3.3). Also shown (*solid line*) is the prediction of the Parker wind model. The density profile of the Parker wind model has been arbitrarily normalized to match the other cases near  $r/r_g \approx 2$ . For comparison, the dotted line in the right panel shows  $n \propto r^{-2}$ .

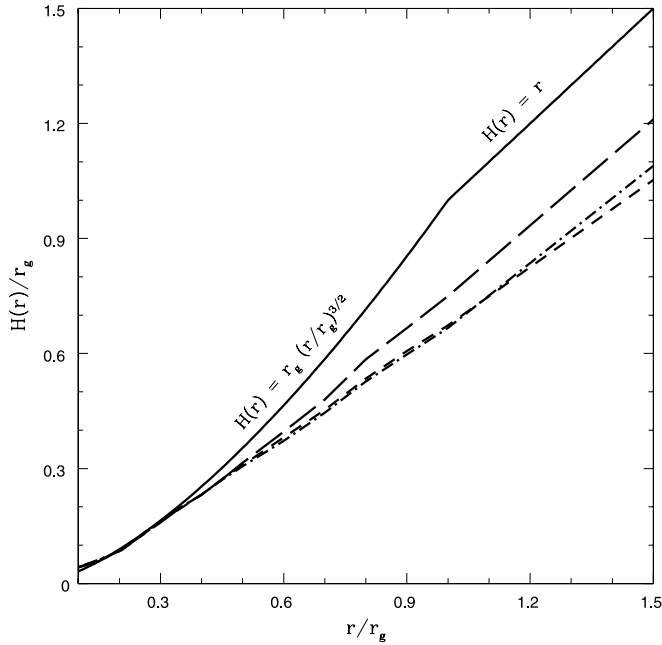


FIG. 5.—Scale height of the ionized atmosphere as a function of disk radius. The solid line shows the analytic result of SJH93 and HJLS94. The short-dashed line represents the  $\alpha = 3/2$  case, the long-dashed line represents the  $\alpha = 5/2$  case, and the dot-dashed line shows the PDW model (see § 3.3).

a number of simplifying assumptions about the form of the atmosphere, especially for the scale height  $H(r)$ . In this section we test whether or not these assumptions are valid.

In the SJH93 and HJLS94 model, the density distribution within  $r_g$ , their “no flow” region, is determined entirely by the base density distribution  $n_0(r)$  and the scale height of the ionized atmosphere  $H(r)$ . Since we assume a base density distribution that is nearly identical to theirs, any differences between the models will manifest themselves in differences between the scale height distributions. Plotted in Figure 5 are the predicted scale height profiles for the  $\alpha = 3/2$  and  $5/2$  cases. Also shown is the analytic result of SJH93 and HJLS94. Reassuringly, each of the cases closely follows the analytic result out to  $r/r_g \sim 0.4$ , matching both the shape and normalization of the analytic result. They each break away from the predicted relation at larger radii. This is not unexpected, since

the identification of  $r_g$  as the launching point for the outflow is only accurate up to an order of unity coefficient. For example, the Parker wind “launches” at  $0.5r_g$  because of pressure gradients in the divergent flow, and the disk wind can produce an even stronger pressure gradient. The fact that the simulations match the analytic result out to  $r/r_g \sim 0.4$  implies that the simulations and analytic model are neither hugely discrepant nor strongly influenced by the base density distribution [at least in determining  $H(r)$ ]. Thus, we are confident that a hydrodynamic model with a shallow base density slope near the star and a steeper density slope at large radii (such as that considered immediately below) will produce a reasonable model of the photoevaporating disks.

### 3.3. Photoevaporative Disk Wind Model

While the  $\alpha = 3/2$  and  $5/2$  cases were used to represent the range of base conditions, neither provides a reasonable fit to the full range of densities at the base of the photoevaporating disk models developed by SJH93 and HJLS94. A better solution is to use a hybrid power-law model, which has a base density profile that mimics the  $\alpha = 3/2$  case at small radii and the  $\alpha = 5/2$  case at large radii. In fact, the radiative transfer calculations of HJLS94 demand such a model. We choose the following fitting function in order to quickly yet smoothly make the transition:

$$n_0(r) = n_g \left[ \frac{2}{(r/r_g)^{15/2} + (r/r_g)^{25/2}} \right]^{1/5}. \quad (10)$$

Alternative fitting functions were tested, and no significant changes in the results below were found. This hybrid model, hereafter the photoevaporative disk wind (PDW) model, is run in ZEUS-2D under the same conditions as the  $\alpha = 3/2$  and  $5/2$  cases, as described in § 3.2.1.

Plotted in Figure 6 are streamlines, velocity, and density contours for the PDW model. A quick comparison of Figure 6 with Figures 1 and 2 reveals that, as expected, the PDW model is intermediate between the  $\alpha = 3/2$  and  $5/2$  cases. However, it more closely resembles the  $\alpha = 5/2$  case. The reason for this is that most of the total mass-loss rate in the PDW model is confined to  $r/r_g \lesssim 2$ , which is very similar to the  $\alpha = 5/2$  case. In addition, both models appear to be approaching spherical

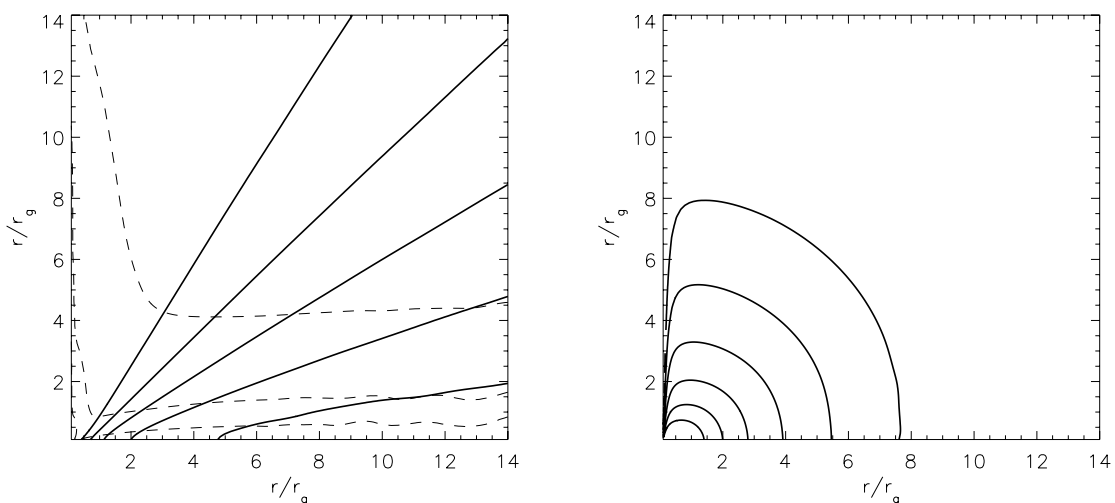


FIG. 6.—Steady state results for the PDW model. The panels and lines have the same meaning as in Fig. 1.

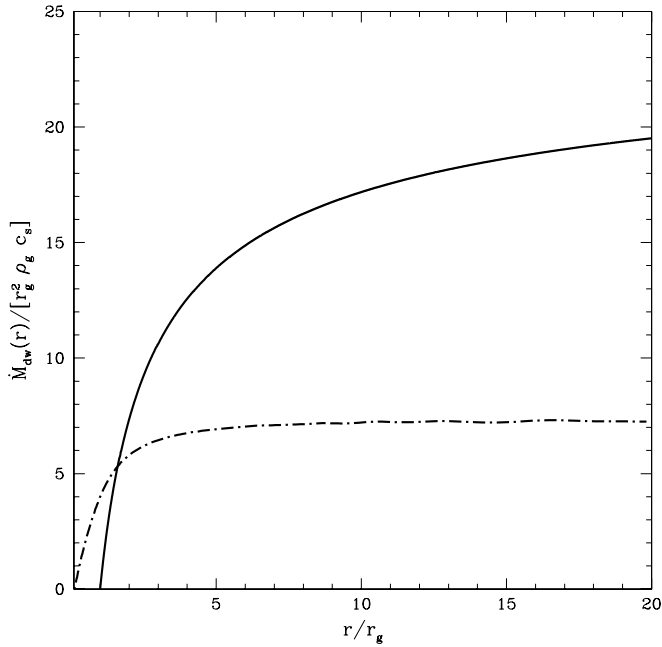


FIG. 7.—Integrated disk wind mass-loss rates as a function of disk radius. The dot-dashed line represents the PDW model, while the solid line represents the analytic result of SJH93 and HJLS94.

symmetry at large radii (the density contours are nearly spherical, while the streamlines are approximately radial). This is an expected result. Figures 4 and 5 compare the results for the PDW model flow against the other two cases and the Parker wind solution.

A physically insightful comparison between the PDW model and the analytic model of SJH93 and HJLS94 is through the integrated mass-loss rate profile. The integrated mass-loss rate along the disk, assuming azimuthal symmetry and for both disk hemispheres, is calculated via

$$\dot{M}_{dw}(r) = 4\pi \int_{0.1r_g}^r \rho(r') v_\theta(r') r' dr'. \quad (11)$$

The mass-loss rate is presented in dimensionless units in Figure 7.

There are two noticeable differences between the PDW model and the analytic result. First, the PDW model shows significant mass loss at radii smaller than  $r_g$ , whereas the analytic model has no mass loss at these radii (by definition). Also clearly evident is that the PDW model predicts a lower total integrated mass-loss rate than the analytic result (by approximately a factor of 2.7). This is due entirely to the velocity of the flow off the disk being much smaller than that assumed by SJH93 and HJLS94 (they assumed the flow velocity to be equal to the sound speed).

The total mass-loss rate is determined by both the base velocity and density. Since the models used here fix the density along the base to be nearly identical to the analytic result of HJLS94, it is the change in the launch velocity that accounts for the difference in the mass-loss rate. Our simulations have outflow velocities in the range of  $\sim(0.3-0.4)c_s$ . As a check, if we assume  $v_\theta = c_s$  and integrate equation (11) from  $r/r_g = 1$  to 20 (to mimic the analytic result), we find a total mass-loss rate that is within 10% of the analytic result.

The velocity profile of the flow is determined primarily from the divergence of the streamlines and depends on density

contrast, not the absolute density. Provided that the density drops as steeply as  $\alpha = 5/2$  in the outer disk, the base velocity should be reasonably well determined by the hydrodynamic simulation. The normalization of the density, however, depends on the detailed balance between incident ionizing radiation, recombinations within the flow, and the liberation of new ions at the base. HJLS94 solved this balance equation explicitly, assuming a constant flow, and found that near  $r_g$ , where the flow develops, recombinations dominate or are comparable to the production of new ions. Thus, the base density varies smoothly through  $r_g$ , with the power-law change reflecting the diminishing importance of overhead redirected ionizing radiation. This may need to be modified somewhat for the present model because of the acceleration of the flow and resulting drop in the number density of ionized hydrogen. Thus, the mass-loss rate presented here should be thought of as a lower limit. Farther from the central star, the new ions liberated at the base of the disk will eventually dominate the detailed balance, resulting in a *steeper* density profile and even less evaporation. The density determinations of HJLS94 are *strengthened* when a lower base velocity is adopted.

What are the implications of our simulations for the study of photoevaporating disks? A primary goal of HJLS94 was to see whether the photoevaporation of neutral disks could replenish the expanding ionized gas in ultracompact H II regions, thus explaining the paradoxical long lifetimes of such systems. In this context, the lifetime of an H II region is inversely proportional to the disk wind mass-loss rate. Since the simulations predict mass-loss rates that are within a factor of 2–3 of the HJLS94 model, our results do not significantly modify the conclusions of these authors. Rather, they reaffirm the importance of the photoevaporation mechanism proposed by HJLS94. The same situation holds for the dispersal of disks around low-mass stars (SJH93; Clarke et al. 2001; Matsuyama et al. 2003a). We do not expect major changes in the conclusions of those papers when these more accurate dispersal values are used. Only the details of how the disk evolves near  $r_g$ , where the hydrodynamic simulations show the strongest disagreement with the analytic theory, should be affected. Thus, the importance of a gap forming within the disk around  $r_g$  and preventing planetary migration may need to be recalculated (Matsuyama et al. 2003b).

After the work of SJH93 and HJLS94 there were a number of published observational studies on low-velocity outflows in young stellar systems. Most notable of these is the T Tauri survey of HEG95. Below, we consider the observational consequences of our simulations for photoevaporating disks around young, low-mass T Tauri stars. We then compare our results with the observational data of HEG95. This is the focus of § 4. We show that the simulations generally give reasonable fits to a number of observed trends.

#### 4. OBSERVATIONAL CONSEQUENCES AND COMPARISON WITH HEG95

The most common way to constrain the properties of low-velocity outflows from T Tauri stars is through observations of forbidden emission lines (typically, optical lines). Commonly measured lines include [S II]  $\lambda 6731$ , [S II]  $\lambda 6716$ , [N II]  $\lambda 6583$ , [O I]  $\lambda 6300$ , and [O I]  $\lambda 5577$ . Here we explore the predicted profiles and strengths of such lines from our simulations and how these depend on, for example, the inclination angle of the system and the region of the system being observed (in the event the system is resolved). We also compare the model results with the observational data of HEG95.

#### 4.1. Rescaling for T Tauri Systems

Before line profiles and luminosities can be calculated, the simulations must be scaled from dimensionless units into physical units. The three fundamental quantities that must be rescaled are the velocity of the gas, the density of the gas, and the size of the system.

First, the velocity of the gas is rescaled by considering that for a gas with a solar abundance of elements and a temperature of  $10^4$  K, the sound speed  $c_s$  is  $\approx 10$  km s $^{-1}$ . The physical size of the system is calculated by rescaling  $r_g$ . Assuming a sound speed of 10 km s $^{-1}$ , the value of  $r_g$  is given by

$$r_g \approx 1.3 \times 10^{14} \left( \frac{M_*}{1 M_\odot} \right) \text{ cm}. \quad (12)$$

In what follows, we focus on systems with  $0.1 M_\odot \leq M_* \leq 2 M_\odot$ , similar to those observed by HEG95.

Finally, we rescale the density of the simulations. As discussed in SJH93 and HJLS94, the value of  $n_g$  is determined by the mass of the star (or, equivalently,  $r_g$ ) and by the rate  $\Phi_*$  of ionizing photons that are emitted by the star:

$$n_g \approx 4 \times 10^4 \left( \frac{M_*}{1 M_\odot} \right)^{-3/2} \left( \frac{\Phi_*}{10^{41} \text{ s}^{-1}} \right)^{1/2} \text{ cm}^{-3}. \quad (13)$$

We assume rates of  $10^{40} \text{ s}^{-1} \leq \Phi_* \leq 10^{42} \text{ s}^{-1}$ , which are compatible with what is expected from T Tauri stars that are accreting gas onto their surfaces (e.g., Matsuyama et al. 2003a). In § 5 we discuss the validity of this assumption.

The forbidden line luminosity  $L$  at a velocity  $u$  is given by

$$L(u) = \frac{1}{\sqrt{2\pi c_s^2}} \int e^{-[(u-\mu)^2/2c_s^2]} \epsilon(n, T) n(\theta, r) \frac{n_s}{n} dV, \quad (14)$$

where  $\mu$  is the velocity shift along the line of sight due to the motion of the gas,  $\epsilon$  is the line emissivity per ion,  $n_s/n$  is the abundance of the atomic species from which the line originates, and  $dV = r^2 \sin \theta d\theta d\phi dr$ . We have assumed that each cell in the simulation emits a Gaussian line profile, which is renormalized by  $(2\pi c_s^2)^{-1/2}$  to give unity when integrated.

The velocity shift  $\mu$  due to a particular cell's motion is given by

$$\mu = [(v_\theta \cos \theta + v_r \sin \theta) \cos \phi - v_\phi \sin \phi] \sin i - (v_r \cos \theta - v_\theta \sin \theta) \cos i, \quad (15)$$

where  $i$  is the inclination angle of the system. The disk is face-on when  $i = 0^\circ$  and edge-on when  $i = 90^\circ$ .

The line emissivity  $\epsilon(n, T)$  is calculated with the software package FIVELEVEL, which was kindly provided by G. Mellema (2003, private communication). This is a key step, since the lines we focus on have markedly different critical densities.

Finally, we assume that our simulations have a typical solar abundance of elements. We adopt the solar abundance ratios of Anders & Grevesse (1989). We also assume that all the atoms are in the ionization state of interest. For example, when calculating the 6731 Å line, we assume that 100% of the sulfur atoms in the disk wind are singly ionized.

Line profiles are constructed by integrating equation (14) over  $r = (0.1-20)r_g$ ,  $\theta = 0^\circ-90^\circ$ ,  $\phi = 0^\circ-360^\circ$  (i.e., one hemisphere only; see the discussion below), and all velocities. Since the simulations are two-dimensional, we assume

azimuthal symmetry in these calculations. Total integrated forbidden line luminosities and surface brightnesses are calculated by integrating equation (14) over all velocities.

#### 4.2. Global Properties: Ionized Forbidden Lines

The majority of observations of T Tauri systems to date are unresolved (e.g., HEG95). The nature of unresolved observations is such that they can be used to directly constrain only the *global* properties of these systems, such as the total forbidden line luminosity and the mean spectrum of the system. Increasingly, however, high-resolution instruments such as the Space Telescope Imaging Spectrograph on board the *Hubble Space Telescope* are resolving nearby systems (e.g., Bacciotti et al. 2000, 2002). In such cases, it is becoming possible to measure *radial* properties, such as forbidden line surface brightness profiles and spatially resolved spectra. Therefore, we are interested in examining both the global and “structural” observational properties of the present PDW model. We examine here (and in § 4.3) the observational consequences in the event the system is unresolved, while in § 4.4 we focus on the observational properties of a resolved system.

Plotted in Figure 8 are the predicted line profiles for the N II and S II lines as a function of inclination angle for the PDW model. The line profiles are calculated assuming  $M_* = 1 M_\odot$  and  $\Phi_* = 10^{41} \text{ s}^{-1}$ . The intensities of the lines have been scaled to make the peaks equal to unity in order to bring out differences in the shifts/shapes of the predicted profiles.

Focusing on the top left panel, we see that all three lines have been shifted to the blue by approximately 10 km s $^{-1}$ . A blueshift is expected, since the disk is face-on, the outflow is moving away from the disk, and only one hemisphere was simulated. Had we simulated both ionized hemispheres, but with no neutral disk in between, we would observe no shift whatsoever. The presence of a thick neutral disk, however, acts as an occulting surface (with effectively infinite optical depth). Since genuine observations also show blueshifts similar to those plotted in Figure 8 (e.g., HEG95), this implies that thick neutral disks are present in these systems.

The two sulfur lines are shifted more to the blue than the nitrogen line (by  $\approx 2$  km s $^{-1}$ ). The reason for this is that the sulfur lines have lower critical densities than the nitrogen line. Thus, they are more sensitive to the outer, low-density regions of the atmosphere, where the gas is flowing at a higher velocity. The widths (FWHM) of the three lines plotted in the top left panel range from  $\approx 26$  to 29 km s $^{-1}$ , with the sulfur lines being slightly wider than the nitrogen line. This can also be attributed to the lower critical densities of the sulfur lines.

Examining the other three panels in Figure 8, it is clear that as the inclination angle increases, the line profiles become slightly wider and less shifted to the blue (see Table 1). As the disk approaches the edge-on orientation, the Keplerian nature of the disk is more observable, and the radial outflow component is no longer solely flowing away from the observer. At  $i = 90^\circ$ , there are equal amounts of gas flowing toward and away from the observer; hence, there is no shift.

How do the predicted line profiles compare with observed profiles? HEG95 found that the forbidden line emission from T Tauri stars could be divided into two components, low-velocity and high-velocity. The high-velocity component correlates well with central jet diagnostics and shows extent in resolved observations. The low-velocity component, however, does not correlate with the central jet diagnostics and appears unresolved in the images. The low-velocity component appears to

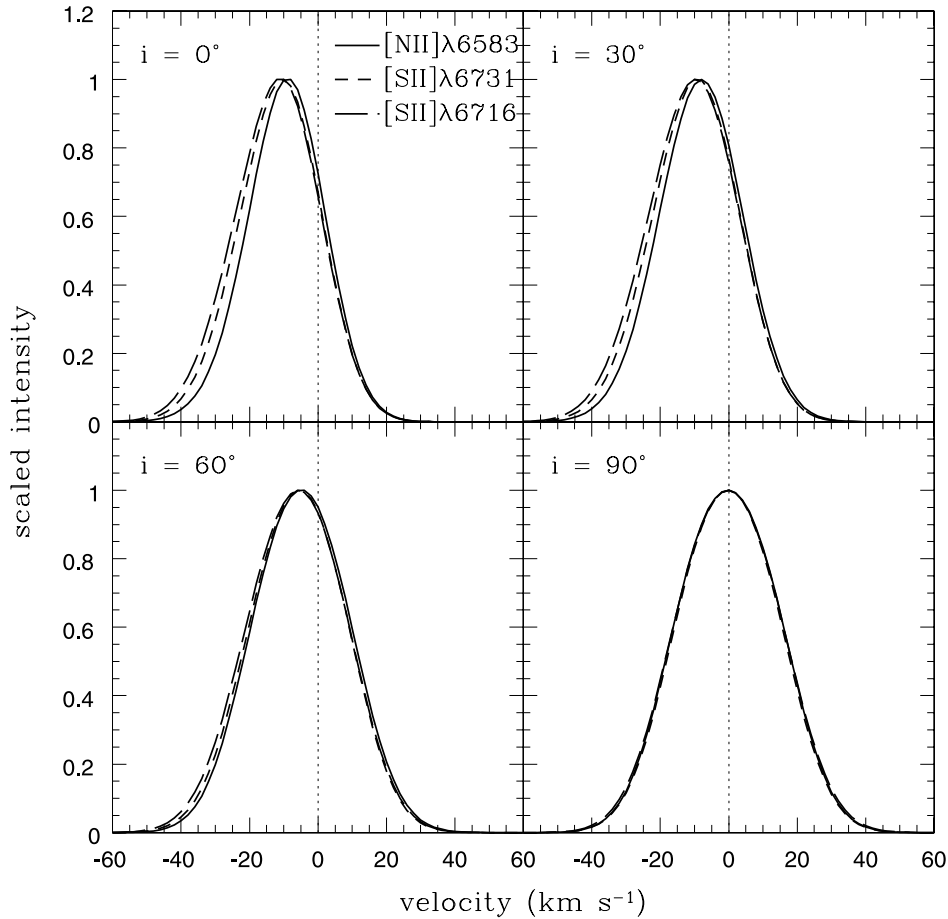


Fig. 8.—Predicted line profiles as a function of inclination angle for the PDW model. The lines have all been arbitrarily normalized so that their peaks are equal to 1.

be associated with a disk wind (Kwan & Tademaru 1988, 1995; Hirth et al. 1997), similar to the winds examined in the present study. Thus, we compare our results with the observed low-velocity component only.

Plotted in Figure 9 is a comparison of predicted and observed [S II]  $\lambda 6731$  line profiles. The predicted line profile is calculated for a face-on PDW model and assumes  $M_* = 1 M_\odot$  and  $\Phi_* = 10^{41} \text{ s}^{-1}$ . We note that changing these parameters (within reason) has only a small effect on the resulting line width and blueshift. The observed profiles were taken from Figure 14 of HEG95. All of the lines (both theoretical and observed) have been scaled such that their peaks are equal to 1. Thus, the plot should be used to compare widths and blueshifts only. A comparison of integrated luminosities is given below.

It is clear that the predicted profile is not a perfect match to the data. The observed lines show a large amount of scatter in

the blueshift of their peaks. However, we find it encouraging that the predicted peak of our profile falls in between and quite close to the peaks of the observed profiles. Our model predicts slightly narrower, line widths than seen in the profiles of DQ Tau and CW Tau (UY Aur is clearly much wider and possibly contains two components). Thus, we would argue that the thermally driven PDW model provides a simple explanation for the kinematics of the observed flows. It would be interesting to understand the slight difference in predicted and observed line widths, however. As indicated by Table 1, an inclined system will give rise to increased line widths. However, this probably cannot explain the difference entirely. Below we argue that a central gap in the disk may be necessary in order to explain the observed luminosities of the N II line at 6583 Å. In terms of flux, a central gap would obviously give more weighting to the high-velocity gas at large radii. As explained in § 4.4, this in turn will give rise to

TABLE 1  
LINE PROPERTIES BY INCLINATION

$i$ (deg)	[N II] $\lambda 6583$		[S II] $\lambda 6731$		[S II] $\lambda 6716$	
	FWHM (km s $^{-1}$ )	Shift (km s $^{-1}$ )	FWHM (km s $^{-1}$ )	Shift (km s $^{-1}$ )	FWHM (km s $^{-1}$ )	Shift (km s $^{-1}$ )
0.....	26.5	-9.2	28.2	-10.9	29.4	-11.8
30.....	28.7	-8.1	29.8	-9.6	31.0	-10.3
60.....	33.2	-4.9	33.2	-5.6	34.2	-6.0
90.....	35.4	0.0	34.9	0.0	35.8	0.0

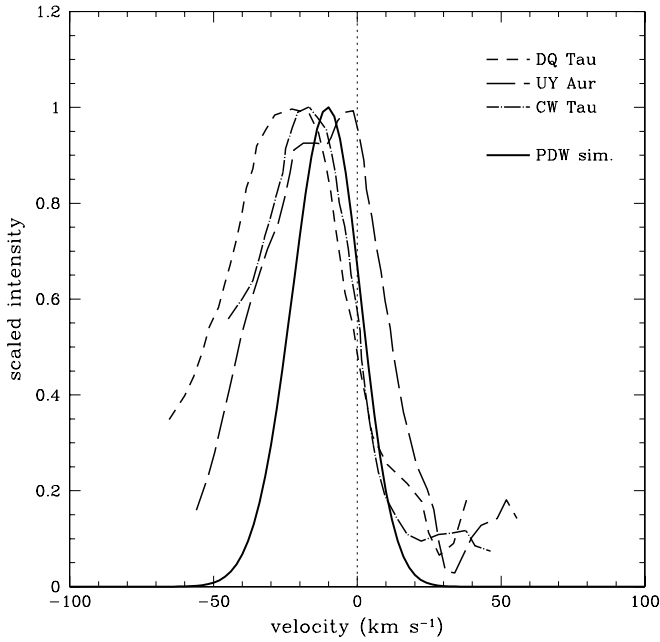


FIG. 9.—Comparison of [S II]  $\lambda 6731$  line profiles. The PDW model profile is calculated assuming  $\Phi_* = 10^{41} \text{ s}^{-1}$ ,  $M_* = 1 M_\odot$ , and  $i = 0^\circ$ .

increased line widths and could possibly explain this slight systematic difference. Alternatively, a small boost from a central “X-wind” (Shu et al. 1994) could also give rise to increased line widths.

Figure 10 presents the integrated line luminosities for the sulfur and nitrogen lines as a function of  $M_*$  and  $\Phi_*$ . Typically, the model predicts luminosities of a few times  $10^{-7}$  up to a few times  $10^{-4} L_\odot$ , with systems that have a higher central stellar mass being more luminous. The trend of higher luminosities with higher central stellar masses (for a fixed value of  $\Phi_*$ ) is easy to understand. If the emissivity per ion,  $\epsilon$ , scales as  $n$  (as would be the case if critical densities were unimportant), we should expect the luminosity to be independent of the mass, since  $L \propto \epsilon n dV \propto n^2 dr^3 \propto M_*^{-3} M_*^3$  (see eqs. [12] and [13]). However, the sulfur and nitrogen lines have critical densities that are comparable to the densities found in the outflow; thus,  $\epsilon$  does not quite scale as the density, and hence  $L \propto M_*^\beta$ , where  $\beta > 0$ . This is confirmed by comparing the N II relation with the S II relations. Note that the N II line luminosity does not depend as strongly on  $M_*$ . The reason for this is that N II has a higher critical density than does S II, and thus a smaller fraction of outflow has densities equal to or exceeding the critical density. It also explains the apparent bends in the  $L$  versus  $M_*$  relations, since the critical densities become less relevant for systems with higher central stellar masses (eq. [13]). The above arguments hold true for fixed values of  $\Phi_*$ , but it is worth noting that  $\Phi_*$  will probably have some mass dependence (e.g., HJLS94). Thus, the two parameters are not entirely independent.

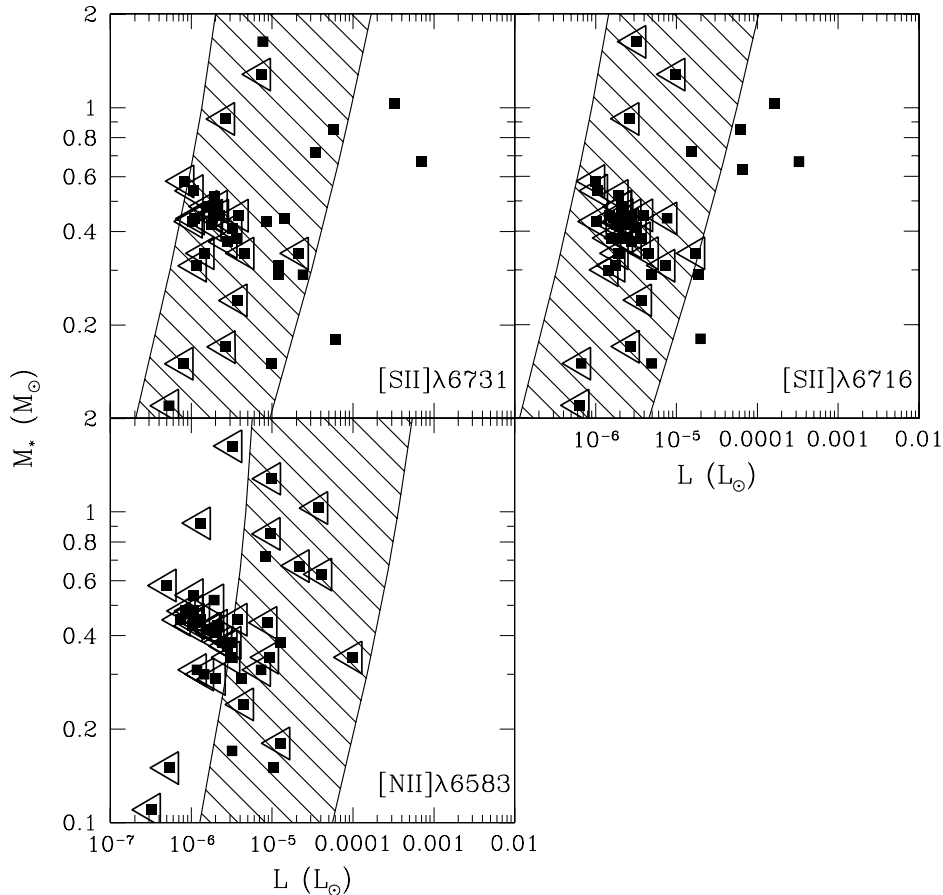


FIG. 10.—Predicted total line luminosities for the disk wind models. The hashed region represents the predictions of the PDW model. The low-luminosity bound is set by assuming  $\Phi_* = 10^{40} \text{ s}^{-1}$  and  $i = 0^\circ$ , while the high-luminosity bound is set by assuming  $\Phi_* = 10^{42} \text{ s}^{-1}$  and  $i = 90^\circ$ . Filled squares show the observational data of HEG95, which are discussed in § 5. Open triangles pointing to low luminosities indicate upper limits.

A comparison with the observational results of HEG95 is also presented in Figure 10. For the data we use the equivalent widths of the observed S II, N II, and O I forbidden lines (in Table 4 of HEG95) to compute the observed integrated luminosities. We note that these equivalent widths were derived from the low-velocity component only ( $-60 \text{ km s}^{-1} < u < 60 \text{ km s}^{-1}$ ), which is appropriate for this comparison, since we have not included jets in our hydrodynamic simulations.

The top panels of Figure 10 illustrate that the PDW model predicts S II luminosities that are in excellent agreement with the observational data of HEG95. This is remarkable, given that the observed systems span more than an order of magnitude in  $M_*$  and more than 2 orders of magnitude in  $L$  and that there was essentially no fine-tuning of the model parameters.

The agreement with the observed N II luminosities (Fig. 10, *bottom*), however, is not as good. In particular, our model tends to be overluminous with respect to the data. Can the difference between the model and data for the N II line be reconciled without spoiling the excellent agreement between the observed and predicted S II luminosities? As noted before, the N II line has a higher critical density than the S II lines. Thus, it is more sensitive to the central regions of the disk wind than are the S II lines. A potential way of reconciling both the N II and S II lines simultaneously is if the central region of the ionized disk atmosphere is either less dense than assumed by our PDW model or entirely removed from the system. HJLS94 considered the effect that strong central winds might have on the structure of the ionized disk atmosphere and concluded that although the inner disk atmosphere might be severely limited, the outer evaporating disk would not be severely affected. Thus, it is possible that the absence of a strong, low-velocity N II component in the observations is evidence for the lack of an inner ionized atmosphere.

#### 4.3. Global Properties: Neutral Forbidden Lines

We have purposely left the discussion of O I forbidden emission lines until now. This is because accounting for the observed line strength of [O I]  $\lambda 6300$  and [O I]  $\lambda 5577$  is difficult in the PDW model, since most of the oxygen in the wind should be ionized. Indeed, the similarity in the ionization potential of both hydrogen and oxygen, and the ensuing charge exchange between the two species, should ensure that the fraction of neutral oxygen is similar to the fraction of neutral hydrogen (Osterbrock 1989). Thus, only at the location where the disk wind crosses the ionization front might one expect to find significant O I emission. Given that the critical densities for these lines are even higher than for nitrogen, the line emission is dominated by the dense gas residing in the interior of the disk and near the base of the disk, just the location where the oxygen may be significantly neutral. Therefore, it is not immediately clear that the present model is completely incapable of explaining the observed O I emission.

Indeed, externally evaporated disks are observed to produce strong O I emission (Bally et al. 1998) that is spatially confined to both the surface of the disk and the ionization front, with about equal total intensity in each component. The disk O I emission must therefore arise within the photodissociation region (PDR) of the flow, below the zone where the ionizing (EUV) photons penetrate.

Störzer & Hollenbach (1998) provide an explanation for this strong O I emission from externally evaporated disk surfaces. Theoretical calculations of the dissociation of oxygen from OH (van Dishoeck & Dalgarno 1983) reveal that a

significant fraction of the oxygen is left in an excited state. Störzer & Hollenbach determine the dissociation rate of OH and calculate the resulting O I line luminosity. The enhanced far-ultraviolet (FUV) radiation field, due to the proximity of a massive star, and the high number density within the PDR produce a strong O I signature, with an [O I]  $\lambda 6300$  surface brightness of  $2.2 \times 10^{-2} \text{ ergs s}^{-2} \text{ sr}^{-1}$ . For typical disk sizes of 100 AU, this results in a total line luminosity of  $\sim 10^{-4} L_\odot$ . These values provide excellent agreement with the observations of Bally et al. (1998). However, because the O I layer is confined to the base atmosphere, where the outflow velocities are smallest, the resulting lines are likely to have only modest blueshifts.

Störzer & Hollenbach (2000) discuss the modification of the externally evaporating disk model for the case of disks evaporated by their central stars and determine that the FUV radiation field is not strong enough to provide significant O I line luminosities. This result, however, does not take into account the possibility of an ionized atmosphere redirecting EUV photons toward the disk. Indeed, the photoevaporating disk model of SJH93 and HJLS94 requires the existence of a dense PDR sandwiched between the ionized wind and the molecular disk.

We check this idea quantitatively for the PDW model. The EUV photons come from a 10,000 K source, and most will have energies near the Lyman limit of 13.6 eV. The cross section for hydrogen atoms to absorb these photons is of the order of  $5 \times 10^{-18} \text{ cm}^2$ . Thus, the EUV photons penetrate a neutral column of  $\approx 2 \times 10^{17} \text{ cm}^2$ . This means that the ionization front, the region where the gas is still 10,000 K but has a significant fraction of neutral oxygen and hydrogen, has a column density of H atoms of  $\approx 2 \times 10^{17} \text{ cm}^2$ . We have determined the zone at the base of atmosphere in the PDW simulation that contains this column density for a range of stellar masses and ionizing photon rates. Typically, we find that the predicted blueshifts are of the order of 3–4  $\text{km s}^{-1}$ , which compares quite favorably with the observations of HEG95 (they find an average offset of  $\sim 5 \text{ km s}^{-1}$  for neutral oxygen lines), but the integrated luminosities are only of the order of  $10^{-7}$  to  $10^{-6} L_\odot$ , which is about 2 orders of magnitude lower than observed (HEG95). Thus, without some kind of modification, the present model cannot easily accommodate the strength of the observed O I emission from T Tauri stars.

#### 4.4. Radial Properties

A potentially powerful test of the model, which will be possible within the coming years, is through comparisons with observed structural properties. Plotted in Figure 11 are predicted nitrogen and sulfur line profiles as a function of projected radius for the face-on PDW model. The lines are calculated assuming  $M_* = 1 M_\odot$  and  $\Phi_* = 10^{41} \text{ s}^{-1}$ . Each of the lines have been normalized such that the peak of the line profile for the entire system, i.e., for  $(0-20)r_g$ , is unity. Thus, in addition to showing how the shapes of the line profiles change as a function of projected radius, the plots indicate how the various regions of the disk contribute to the mean spectrum of the system.

Focusing on the shapes of the profiles in the three panels, it is clear that as one goes farther from the projected center of the outflow, the profiles become more skewed. In particular, at large projected radii there are “wings” evident on the blue sides of the profiles. The development of line wings has a physical explanation. At small projected radii from the center,

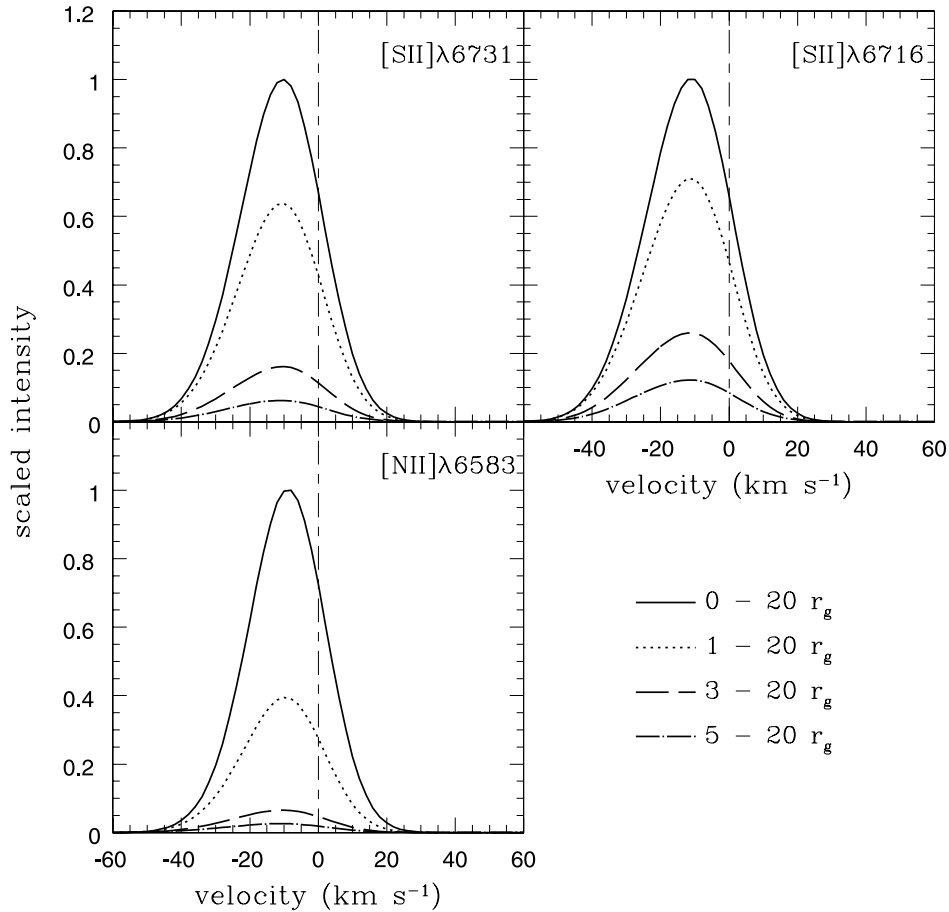


FIG. 11.—Predicted line profiles as a function of radius for the face-on ( $i = 0^\circ$ ) PDW model. The lines have all been normalized so that the peak of the  $(0-20)r_g$  line (i.e., the entire disk) equals 1.

most of the flux from the system originates from the dense ionized disk. Because the velocity of the gas flowing off the ionized disk is fairly constant as a function of radius, a nearly perfect Gaussian line profile is the result. Since most of the flux comes from the central regions of the outflow, this also explains why the mean spectrum of the entire system is almost exactly Gaussian. However, as one moves to larger projected radii, the role of the atmosphere above the disk, in terms of flux, becomes more important. The gas in the atmosphere is flowing faster than the gas near the ionized disk (e.g., Fig. 6, *left*); hence, the Gaussian profile is skewed toward the blue. The increased importance of the atmosphere at large projected radii also causes the peak of the line profile to shift farther to the blue and the FWHM of the line to increase. We demonstrate this quantitatively by fitting Gaussians to the line profiles. The results are presented in Table 2. While the shift in

the peak is modest ( $\sim 2 \text{ km s}^{-1}$ ) in going from the mean spectrum of the system to just focusing on the outer regions of the system, the increase in the line width is actually fairly substantial ( $\geq 15\%$ ) and potentially observable.

It is also evident in Figure 11 that the nitrogen line produces a larger fraction of its total flux from the central region of the outflow than either of the sulfur lines. The reason for this trend is that the nitrogen line is more sensitive to the high-density regions of the atmosphere than are the sulfur lines.

Finally, plotted in Figure 12 are the predicted surface brightness profiles for the sulfur and nitrogen lines. These are also calculated assuming  $M_* = 1 M_\odot$  and  $\Phi_* = 10^{41} \text{ s}^{-1}$ . The surface brightness profiles of the three lines all exhibit the same general features: a central core and a power-law drop off at large radii. The size of the core is dictated by the critical densities of the lines, with the N II profile being the most

TABLE 2  
LINE PROPERTIES BY REGION

REGION	[N II] $\lambda 6583$		[S II] $\lambda 6731$		[S II] $\lambda 6716$	
	FWHM ( $\text{km s}^{-1}$ )	Shift ( $\text{km s}^{-1}$ )	FWHM ( $\text{km s}^{-1}$ )	Shift ( $\text{km s}^{-1}$ )	FWHM ( $\text{km s}^{-1}$ )	Shift ( $\text{km s}^{-1}$ )
$0-20r_g$ .....	26.5	-9.2	28.2	-10.9	29.4	-11.8
$1r_g-20r_g$ .....	28.0	-10.3	29.2	-11.4	30.4	-12.3
$3r_g-20r_g$ .....	31.6	-11.8	31.5	-11.8	32.5	-12.7
$5r_g-20r_g$ .....	32.8	-12.6	32.7	-12.5	33.1	-13.0

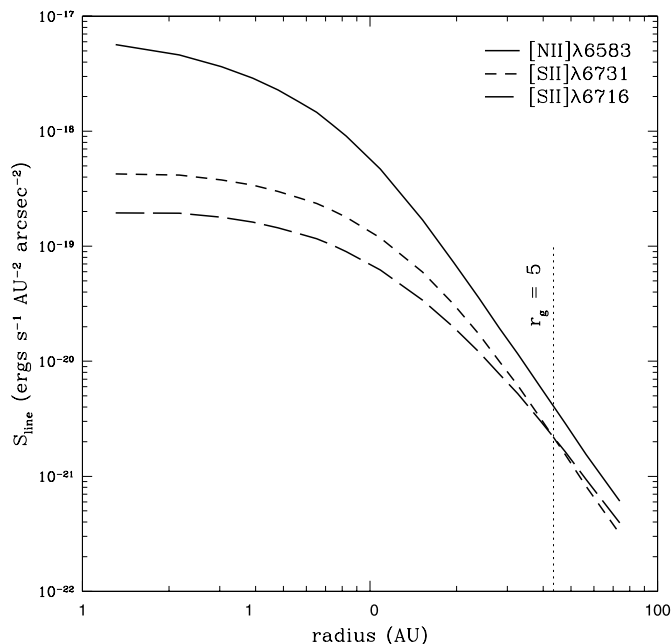


FIG. 12.—Predicted forbidden line surface brightness profiles for the face-on PDW model.

concentrated because of the higher critical density of nitrogen. At large radii, the profiles drop off roughly as  $S_{\text{line}} \propto r^{-3}$ . This can be understood physically, since  $S_{\text{line}} \propto \epsilon n r \propto r^{-2} r^{-2} r$  ( $\epsilon \propto n^{-1}$  at large radii, low densities). The slight differences in the slopes of the three profiles are attributable to differences in the critical densities.

## 5. DISCUSSION AND CONCLUSIONS

The evidence for self-produced photoevaporative disk winds around low-mass stars is largely circumstantial. The primary reason for this has been the lack of detailed calculations on the outflow properties of these winds to compare with observations. Photoevaporative disk wind models have, however, been shown to fit the observational data of externally heated low-mass stars in the vicinity of massive stars (e.g., Johnstone et al. 1998; Bally et al. 1998; Störzer & Hollenbach 1998) because the disk wind geometry and flow characteristics are much simpler.

In this paper we use hydrodynamic simulations to compute the properties of the PDW model and, subsequently, the predicted observational signatures. We show that the hydrodynamic simulations converge to steady state solutions and that a number of general properties (e.g., scale height distribution, integrated disk wind mass-loss rate) agree well with the earlier analytic results of SJH93 and HJLS94. The outflows become nearly spherically symmetric and match the analytic solution to the Parker solar wind problem at large radii, as expected. We further demonstrate that the photoevaporative winds produce blueshifted ionized forbidden lines with typical offset velocities of approximately  $-10 \text{ km s}^{-1}$ , widths of  $\sim 30 \text{ km s}^{-1}$ , and integrated luminosities of  $10^{-7}$  to  $10^{-4} L_{\odot}$ . These values compare favorably with the observations of HEG95 (see Figs. 9 and 10). The strength of the observed O I emission is difficult to account for with the present model, however.

The photoevaporative disk winds examined here are intuitive and physically simplistic. They rely on the availability of  $\Phi_* = 10^{40}$ – $10^{42}$  ionizing photons  $\text{s}^{-1}$  to be emitted by the central star disk accretion shock. Theoretical arguments sup-

port such high levels of ionizing emission (e.g., Matsuyama et al. 2003a). Observationally, it is extremely difficult to directly pin down the value of  $\Phi_*$  for low-mass T Tauri stars. HEG95 measured the mass accretion rates onto the surface of the T Tauri stars, however, and these, in principle, can be used to estimate the value of  $\Phi_*$ . Given the mass accretion rate and the stellar radius, we calculate the accretion shock luminosity of the gas as it falls onto the star’s surface via

$$L_{\text{acc}} = \frac{GM_* \dot{M}_{\text{acc}}}{2R_*}, \quad (16)$$

where  $\dot{M}_{\text{acc}}$  is the mass accretion rate and  $R_*$  is the radius of the T Tauri star (see also Matsuyama et al. 2003a). Using the inferred values of  $L_{\text{acc}}$  and assuming blackbody radiation with a characteristic temperature of 10,000 K (Johns-Krull et al. 2000; Gullbring et al. 2000), we indeed estimate  $\Phi_* \sim 10^{40}$ – $10^{42} \text{ s}^{-1}$ . This lends credence to the photoevaporative wind hypothesis.

Utilizing these ultraviolet photons, however, may be difficult. As mentioned above, both the protostellar jet (Shang et al. 2002) and the accretion column (Alexander et al. 2004) are likely to be optically thick to ionizing radiation, protecting the disk. Nevertheless, energy released within the accretion disk, and in the fast-moving jet, may produce significant ionizing radiation. Alternatively, the disk may be heated by another source such as FUV photons (Johnstone et al. 1998; Störzer & Hollenbach 1998).

The calculations presented here reveal that heating the disk surface to  $10^4$  K will produce a thermal wind with flow characteristics similar to those observed around T Tauri stars. In addition, if the mass-loss rate is high enough, comparable to the evaporating disk model, the forbidden line profiles of S II and N II can be explained. Curiously, if the  $10^4$  K wind is not ionized by EUV photons, the resulting O I forbidden line radiation would also be comparable to that observed. Thus, the observations of HEG95 seem to require a partially ionized  $10^4$  K wind.

Alternative models have also been proposed to explain the observed low-velocity component. In fact, the prevailing view is that T Tauri winds are magnetically driven (e.g., Anderson et al. 2003). This is largely because strong magnetic fields seem to be the only way to power the collimated, high-velocity jets that are responsible for the high-velocity component observed in T Tauri spectra. In addition, magnetic wind models are able to reproduce a number of the observed features of the high-velocity component (e.g., Shang et al. 1998; Garcia et al. 2001a, 2001b). It is less clear, however, whether the magnetic wind models can account for the low-velocity component, which was the subject of investigation in § 4. Below we briefly discuss how the predicted low-velocity components of magnetic wind models compare with their observational counterparts. We argue that the PDW model proposed in the present study matches the current suite of observations at least as well magnetic wind models.

Generally speaking, magnetic wind models can be divided into two classes: *X*-winds (Shu et al. 1994) and disk winds (Blandford & Payne 1982). The primary difference between these two classes is the physical extent of the magnetic field and, therefore, the location of the outflow launching radius. In *X*-wind models, the magnetic field is contained entirely within the very inner regions of the disk immediately next to the star. Disk wind models, on the other hand, assume that there is a large-scale magnetic field present that extends to several AU. Unfortunately, it is extremely difficult to work out the exact

observational predictions of such models in a self-consistent manner (Garcia et al. 2001a, 2001b). This is one advantage the physically simplistic PDW model has over the magnetic wind models.

While it is difficult to calculate the precise observational characteristics of magnetic wind models, there have been a number of basic predictions made that are testable with current observational data. In terms of the  $X$ -wind models, the predicted launching radius for the disk outflow is extremely close to the star. However, recent high-resolution observations suggest that the low-velocity component probably originates at “large” disk radii (e.g., Bacciotti et al. 2002; Anderson et al. 2003), suggesting that some other mechanism is responsible for the observed low-velocity component. In fact, irrespective of the model, one should expect the outflow velocity to be of the order of the escape velocity at the region where the wind originated. This is a strong argument that the low-velocity component must originate at moderate radii ( $\sim 1$ – $10$  AU).

Magnetic disk wind models, on the other hand, are able to produce both high- and low-velocity components (e.g., Cabrit et al. 1999; Garcia et al. 2001a, 2001b), with the low-velocity component being launched from reasonably large disk radii. Furthermore, such models predict that the high-velocity component is spatially extended, while the low-velocity component is confined within the central (projected) regions of the system, which is in good agreement with observations. However, the problem with disk wind models is that the level of ionization at large disk radius (i.e., at the launching radius) is too low to allow for strong magnetic coupling (e.g., Gammie 1996). Hence, such models tend to underpredict the luminosity of the low-velocity component by a substantial margin (e.g., Garcia et al. 2001a). As we have shown, however, the PDW model presented here (which contains no magnetic field) can naturally produce an outflow that matches a number of observed trends seen in low-mass T Tauri stars, as long as the photons can penetrate from the central star out to large radii (or an external mechanism for producing EUV photons is present). It is possible, however, that *both* photoevaporation and a large-scale magnetic field could be contributing to the low-velocity com-

ponent, especially since the higher level of ionization due to photoevaporation should increase the effectiveness of the magnetic disk wind. This two-component model could possibly explain the relatively large amount of scatter in the forbidden line profiles and luminosities and why some stars apparently show multiple low-velocity components (e.g., UY Aur; see Fig. 9).

In addition, it is likely that an interface with the fast jetlike wind arising from the inner disk will modify these results. HJLS94 modeled the effect of a strong stellar wind on the ionized atmosphere and concluded that only the inner regions would be affected. This suggests that the results of the calculations in this paper would need to be modified only in the central densest regions, resulting in somewhat lower line fluxes. This would predominantly affect transitions with high critical densities, such as the nitrogen line. Moreover, Matsuyama et al. (2003a) found that gaps could form in the inner part of the disk, near  $r_g$ , because of the erosive power of photoevaporation coupled to the viscous evolution of the disk. Although the Matsuyama et al. models should be recalculated, taking into account the results of this paper, these gaps would remove the inner densest part of the ionized atmosphere produced in this paper. An evolutionary sequence might be visible in the low-velocity spectra from T Tauri stars depending on the state of the underlying disk. Detailed calculations, taking into account each of these factors, should be undertaken.

The authors wish to thank the referee, David Hollenbach, for suggesting significant improvements to the paper. Thanks also to G. Mellema for providing his software package for calculating forbidden line emissivities. I. G. M. thanks A. Babul for useful discussions. A. F. acknowledges financial support from J. F. Navarro. I. G. M. is supported by a postgraduate scholarship from the Natural Sciences and Engineering Research Council of Canada (NSERC). The research of D. J. has been supported by an NSERC Discovery Grant. D. R. B. thanks NSERC for financial support.

#### REFERENCES

- Alexander, R. D., Clarke, C. J., & Pringle, J. E. 2004, *MNRAS*, 348, 879  
 Anders, E., & Grevesse, N. 1989, *Geochim. Cosmochim. Acta*, 53, 197  
 Anderson, J. M., Li, Z. Y., Krasnopolsky, R., & Blandford, R. 2003, *ApJ*, 590, L107  
 Bacciotti, F., Mundt, R., Ray, T. P., Eisloffel, J., Solf, J., & Camezind, M. 2000, *ApJ*, 537, L49  
 Bacciotti, F., Ray, T. P., Mundt, R., Eisloffel, J., & Solf, J. 2002, *ApJ*, 576, 222  
 Bally, J., O’Dell, C. R., & McCaughrean, M. J. 2000, *AJ*, 119, 2919  
 Bally, J., Sutherland, R. S., Devine, D., & Johnstone, D. 1998, *AJ*, 116, 293  
 Blandford, R. D., & Payne, D. G. 1982, *MNRAS*, 199, 883  
 Cabrit, S., Ferreira, J., & Raga, A. C. 1999, *A&A*, 343, L61  
 Clarke, C. J., Gendrin, A., & Sotomayor, M. 2001, *MNRAS*, 328, 485  
 Gammie, C. F. 1996, *ApJ*, 457, 355  
 Garcia, P. J. V., Cabrit, S., Ferreira, J., & Binette, L. 2001a, *A&A*, 377, 609  
 Garcia, P. J. V., Ferreira, J., Cabrit, S., & Binette, L. 2001b, *A&A*, 377, 589  
 Gullbring, E., Calvet, N., Muzerolle, J., & Hartmann, L. 2000, *ApJ*, 544, 927  
 Haisch, K. E., Jr., Lada, E. A., & Lada, C. 2001, *ApJ*, 553, L153  
 Hartigan, P., Edwards, S., & Ghandour, L. 1995, *ApJ*, 452, 736 (HEG95)  
 Hartmann, L., Calvet, N., Gullbring, E., & D’Alessio, P. 1998, *ApJ*, 495, 385  
 Hirth, G. A., Mundt, R., & Solf, J. 1997, *A&AS*, 126, 437  
 Hollenbach, D., Johnstone, D., Lizano, S., & Shu, F. 1994, *ApJ*, 428, 654 (HJLS94)  
 Hollenbach, D., Yorke, H. W., & Johnstone, D. 2000, in *Protostars and Planets IV*, ed. V. Mannings et al. (Tucson: Univ. Arizona Press), 401  
 Jayawardhana, R., Luhman, K. L., D’Alessio, P., & Stauffer, J. R. 2002, *ApJ*, 571, L51  
 Johns-Krull, C. M., Valenti, J. A., & Linsky, J. L. 2000, *ApJ*, 539, 815  
 Johnstone, D., Hollenbach, D., & Bally, J. 1998, *ApJ*, 499, 758  
 Kwan, J., & Tademaru, E. 1988, *ApJ*, 332, L41  
 ———. 1995, *ApJ*, 454, 382  
 Lada, C. J., Muench, A. A., Haisch, K. E., Jr., Lada, E. A., Alves, J. F., Tollestrup, E. V., & Willner, S. P. 2000, *AJ*, 120, 3162  
 Lee, C. F., Stone, J. M., Ostriker, E. C., & Mundy, L. G. 2001, *ApJ*, 557, 429  
 Matsuyama, I., Johnstone, D., & Hartmann, L. 2003a, *ApJ*, 582, 893  
 Matsuyama, I., Johnstone, D., & Murray, N. 2003b, *ApJ*, 585, L143  
 Osterbrock, D. E. 1989, *Astrophysics of Gaseous Nebulae and Active Galactic Nuclei* (Mill Valley: Univ. Science Books)  
 Parker, E. N. 1963, *Interplanetary Dynamical Processes* (New York: Interscience)  
 Shang, H., Glassgold, A. E., Shu, F. H., & Lizano, S. 2002, *ApJ*, 564, 853  
 Shang, H., Shu, F. H., & Glassgold, A. E. 1998, *ApJ*, 493, L91  
 Shu, F., Johnstone, D., & Hollenbach, D. 1993, *Icarus*, 106, 92 (SJH93)  
 Shu, F., Najita, J., Ostriker, E., Wilkin, F., Ruden, S., & Lizano, S. 1994, *ApJ*, 429, 781  
 Stone, J. M., Mihalas, D., & Norman, M. L. 1992, *ApJS*, 80, 819  
 Stone, J. M., & Norman, M. L. 1992a, *ApJS*, 80, 753  
 ———. 1992b, *ApJS*, 80, 791  
 Störzer, H., & Hollenbach, D. 1998, *ApJ*, 502, L71  
 ———. 2000, *ApJ*, 539, 751  
 van Dishoeck, E. F., & Dalgarno, A. 1983, *J. Chem. Phys.*, 78, 4552